Two-dimensional metal–organic polymers as cathode hybrid materials for high-performance Al-batteries

Dawid Pakulski, Verónica Montes Garcia, Adam Gorczyński, Wlodzimierz Czepa, Tomasz Chudziak, Michal Bielejewski, Andrzej Musial, Ignacio Pérez-Juste, Paolo Samorì, Artur Ciesielski

▶ **To cite this version:**

Dawid Pakulski, Verónica Montes Garcia, Adam Gorczyński, Wlodzimierz Czepa, Tomasz Chudziak, et al.. Two-dimensional metal–organic polymers as cathode hybrid materials for high-performance Al-batteries. Journal of Materials Chemistry A, 2023, 12 (1), pp.440-450. 10.1039/D3TA05730E . hal-04354787

HAL Id: hal-04354787
https://hal.science/hal-04354787

Submitted on 19 Dec 2023

HAL is a multi-disciplinary open access archive for the deposit and dissemination of scientific research documents, whether they are published or not. The documents may come from teaching and research institutions in France or abroad, or from public or private research centers.

L'archive ouverte pluridisciplinaire **HAL**, est destinée au dépôt et à la diffusion de documents scientifiques de niveau recherche, publiés ou non, émanant des établissements d'enseignement et de recherche français ou étrangers, des laboratoires publics ou privés.

ARTICLE

Received 00th January 20xx,
Accepted 00th January 20xx

DOI: 10.1039/x0xx00000x

Two-dimensional metal-organic polymers as cathode hybrid materials for high-performance Al-batteries

Dawid Pakulski,[a,b‡] Verónica Montes-García,[c‡] Adam Gorczyński,[d] Włodzimierz Czepa,[b,d] Tomasz Chudziak,[b,d] Michał Bielejewski,[e] Andrzej Musiał,[e] Ignacio Pérez-Juste,[f] Paolo Samorì,[c*] Artur Ciesielski[b,c*]*

Organic materials represent a promising alternative to critical raw materials for energy storage applications due to their sustainable production combined with tunable structures and functionalities. Unfortunately, the biggest limitation of the organic materials is their high solubility in aqueous electrolytes, which results in a poor cycling stability. Metal-organic polymers (MOPs) have emerged as versatile organic materials which exhibit enhanced chemical stability as well as redox activity depending on the employed building units. Here, by mastering a coordination chemistry approach, two novel MOPs were synthesized *via* a coordination process between tetraminobenzoquinone (TABQ) with a metal ion (*i.e.,* zinc or copper) and were explored as cathode materials for aluminum-ion batteries. The resulting Zn-TABQ MOP exhibited superior electrochemical performance compared to other common cathode materials in Al-batteries. Specifically, Zn-TABQ revealed a specific capacity of 198 mAh/g at 0.05 A/g, combined with high-capacity retention (92%) after 5000 cycles at a scan rate of 1 A/g and an outstanding energy density of 247 Wh/kg. We demonstrated *via* ex situ characterization that the electrochemically-active carbonyl (C=O) units of Zn-TABQ coordinate the $AlCl_2^+$ and $EMIM^+$ ions, thereby governing the mechanism of ion storage and release by taking advantage of the nature of the reversible interaction.

Introduction

The unavoidable transition from fossil fuels to renewable energy sources together with the ever-growing worldwide energy demand have triggered the search for novel and efficient energy storage systems (ESS) that can support the transition and the energy supply for on-demand utilization.[1-4] Since their first commercialization by Sony in 1991, lithium-ion batteries (LIBs) have dominated the electronics market. However, the limited and uneven distribution of lithium reserves across the globe has been recently acknowledged by EU Monitor in 2020, which identified lithium for the first time as critical raw material (CRM),[5] sparking the development of ESS alternatives relying on the use of Na^+, K^+, Mg^+, Al^{3+}, Zn^{2+}, etc.[6]

[a] *Adam Mickiewicz University Foundation, Poznań Science and Technology Park, Rubież 46, 61-612 Poznań, Poland*
[b] *Centre for Advanced Technologies, Adam Mickiewicz University, Uniwersytetu Poznańskiego 10, 61-614 Poznań, Poland*
[c] *Université de Strasbourg, CNRS, ISIS 8 allée Gaspard Monge, 67000 Strasbourg, France*
[d] *Faculty of Chemistry, Adam Mickiewicz University, Uniwersytetu Poznańskiego 8, 61-614 Poznań, Poland*
[e] *Institute of Molecular Physics, Polish Academy of Sciences, M. Smoluchowskiego 17, 60-179 Poznan, Poland*
[f] *Departamento Química Física, Universidade de Vigo, 36310 Vigo, Spain*

†Electronic Supplementary Information (ESI) available: [details of any supplementary information available should be included here]. See DOI: 10.1039/x0xx00000x

Among them, rechargeable aluminum-ion batteries (RABs) appear particularly appealing and exhibit several its environmental sustainability and limited cost,[7] as Al is the most abundant metal in the Earth's crust (~8%) and the price of its raw materials (*i.e.,* aluminium silicates) is also the lowest (1.9 USD/kg) compared to other metals suitable for their use in ESS.[8] Al exhibits the highest theoretical volumetric capacity at 8,046 mAh/cm^3 and its theoretical gravimetric capacity (2,981 mAh/g) is very close to that of Li (3,861 mAh/g).[9] Besides, RABs exhibit significant advantages compared with batteries relying on other metals such as the safety and nontoxicity of Al. Furthermore, multivalent metals are less prone to dendrite formation, which opens the possibility for their practical application as metal anodes.[6] In their ground-breaking work in 2015 Dai *et al*. reported the use of 3D graphitic foam as cathode, Al anode and $AlCl_3$–EMIMCl (EMIMCl: 1-ethyl-3-methylimidazolium chloride) chloroaluminate ionic liquid (IL) as electrolyte. This room-temperature RAB delivered a capacity of 60 mAh/g with 97% coulombic efficiency (CE) for over 7500 cycles.[10] Although graphite-based positive electrodes exhibit considerable cycling stability, the Al-storage mechanism is mainly based on the intercalation/deintercalation of $AlCl_4^-$ anions in the graphite layer, and therefore the capacity will always remain limited by the amount of electrolyte, resulting in rather modest cell energy densities.[11] Therefore, to boost the device's energy density, the design of novel electrode materials for Al storage becomes essential.

Organic electrode materials represent a powerful alternative for further improving the electrochemical performance of RABs, not only

Please do not adjust margins

because of their high theoretical capacities, sustainable production and structural tunability but also because they can store Al ions through a coordination reaction mechanism.[12-15] Conjugated carbonyl (C=O) compounds (*i.e.,* quinones and their derivatives) have been identified as highly promising redox-active materials due to their highly reversible electrochemical performance.[16-19] Upon electrochemical reduction of carbonyl compounds, negatively charged oxygen atoms coordinate with positively charged Al-complex ions (*e.g.,* Al^{3+}, $AlCl_2^+$ or $AlCl^{2+}$), in a reversible process driven by the oxidation.[6, 9, 16, 20, 21] For instance, Lin *et al.*, employed tetraamino-*p*-benzoquinone (TABQ) as cathode material for aqueous zinc-organic batteries, which has been characterized by a high capacity of 303 mAh/g at 0.1 A/g.[22] Unfortunately, the partial solubility TABQ in the aqueous electrolyte (1M $ZnSO_4$) renders insufficient cycle life (< 1000 cycles) for commercial applications.[22]

Metal-organic polymers (MOPs) have emerged as versatile organic materials for ESS due to their easily tunable structures, chemical stability, mechanical flexibility, low cost and well-dispersed single metal sites.[23-28] The flexibility of polymeric materials makes it possible to insert/extract ions rapidly without significant volume change and therefore MOPs are capable of achieving fast ionic intercalations.[29] In addition, their pore size, surface area and electrochemical activity can be easily tuned by the suitable choice of metal ions and organic ligands. MOPs based on the coordination of TABQ with Ni, Fe or Co metal ions have been explored in Na ion batteries, Li ion batteries and Li–O_2 batteries, respectively.[23, 24, 30] Lv *et al.*, synthesized a semiconducting Co-TABQ MOP, which exhibited a broadly intensive visible-light absorption and can be employed as a photoelectrode in Li-O_2 battery.[23] On the other hand, Ni-TABQ and Fe-TABQ have been explored as cathode materials in Na and Li ion batteries, respectively, delivering high capacities of 469.5 mAh/g (Ni-TABQ) and 251.1 mAh/g (Fe-TABQ).[24, 30] However, the cycling performance of these materials was only assessed for 450 and 200 cycles respectively. Besides, although the charge storage mechanism of TABQ was elucidated in both cases, the role of the different metal ions has not been investigated. We envisage that the selected metal ions can provide a capacitive contribution to the charge storage mechanism of TABQ-based MOPs. Among all metal ions, zinc and copper appear being the ideal alternative, not only because their salt precursors have the lowest prices (3,031 and 6,836 USD/T respectively), but also are envisaged to induce a higher theoretical capacity due to their higher atomic weight. Importantly, to the best of our knowledge, the great potential of MOPs based on TABQ coordinated with Zn or Cu ions for energy storage applications remains unexplored.

Herein, we report on the synthesis of two novel MOPs, *i.e.*, Zn-TABQ and Cu-TABQ, *via* the coordination of a redox-active TABQ monomer with a bivalent metal ion (*i.e.,* zinc or copper). These two metal ions with different degrees of filled *d*-shell orbitals (d^9 – Cu^{2+}; d^{10} – Zn^{2+}) were chosen to explore and correlate the resulting chemical structures with their chemical stability and their electrochemical performance. The electrochemical performance of Zn- and Cu-TABQ MOPs is first assessed in a three-electrode system as well as in a symmetric system by using EMIM ionic liquid as electrolyte. The influence of surface area, pore size, ionic conductivity, and the presence/absence of oxidation/reduction of the metal ion in the two MOPs on the specific capacitance and long-term cyclability has been assessed. As practical application, a rechargeable Al ion battery is assembled, in which Zn-TABQ or Cu-TABQ are used as cathode materials, Al as anode and $AlCl_3$–[EMIM]Cl IL as electrolyte. Finally, ex situ Fourier-transform infrared (FTIR), Raman and X-ray photoelectron (XPS) spectroscopies together with DFT calculations are used to shed light onto the charge storage mechanism of Al-complex ions by the Zn-TABQ cathode materials.

Results and discussion

Synthesis and structural characterization

Metal-organic polymers (MOPs) based on the coordination of TABQ with Zn^{2+} and Cu^{2+} metal ions are assembled using a facile wet chemical synthesis, where TABQ reacts with an equimolar amount of Zn^{2+} or Cu^{2+} in a solution of ammonia and dimethylsulfoxide (DMSO) at room temperature, as shown in Fig. 1 (See experimental section for details).

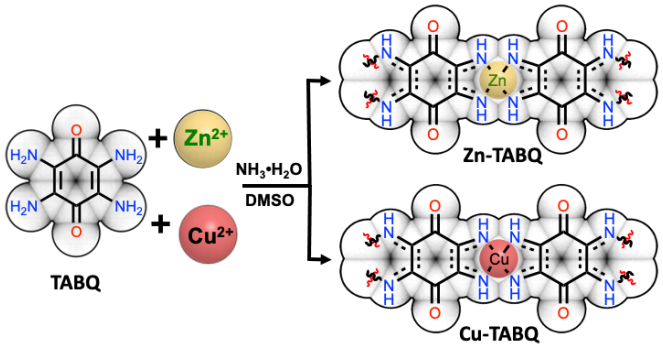

Fig. 1. Synthetic pathway of Zn-TABQ and Cu-TABQ MOPs.

The chemical structures of the Zn- and Cu-TABQ MOPs are confirmed by means of Direct Polarization (DP-MAS) and Cross Polarization Magic Angle Spinning (CP-MAS) solid-state NMR spectroscopy (See Fig. 2a and S1†). C^{13} NMR DP-MAS analyses of Zn- and Cu-TABQ show two major signals at 159 and 167 ppm respectively, which correspond to the carbons in the C=N and C=O bonds. Other peaks present in both the spectra of MOPs (chemical shifts 90-130 ppm and ~40 ppm) can be ascribed to the aromatic structure of each MOP and to C-N bonds, respectively. The mechanism responsible for relaxation in the CP-MAS solid-state is driven in most cases by local magnetic field fluctuations as well as by dipole-dipole interactions.[31, 32] The presence of diamagnetic ions (*e.g.*, Zn^{2+}) in the structure does not influence in a significant way the relaxation mechanisms driven by dipolar interactions between spins (Fig. S1a†). However, Cu^{2+} ions, which are paramagnetic centers, lead to a very effective and fast relaxation mechanism caused by electron-dipole interaction, which shortens the relaxation times significantly and lead to a flat NMR CP-MAS spectrum (Fig. S1b†).[33, 34]

The coexistence of the stretching vibrations of C=N at 1139 and 1577 cm^{-1} in the Raman spectra of the Zn- and Cu-TABQ (See Fig. 2b) confirms the electron redistribution on the nitrogen atoms as a result of their coordination with Zn^{2+} or Cu^{2+}. Moreover, this coordination also leads to the appearance of two novel peaks around ~400 cm^{-1}, which are not present in the Raman spectrum of TABQ (See Fig. S2†) and correspond to metal-nitrogen bonds.[24]

Similarly, Fourier transformed infrared spectroscopy (FTIR) analysis reveals the characteristic stretching vibrations of -NH around 3300 cm^{-1} of pure TABQ as well as after the coordination with the Zn^{2+} and Cu^{2+} metal ions (See Fig. S3†). The vibration of the carbonyl bond (C=O) in Zn-TABQ and Cu-TABQ is blue-shifted from 1664 to 1580 and 1602 cm^{-1}, respectively, due to the coordination effect and the attraction between chains.[35] The hydrogen bond between the oxygen atoms of benzoid carbonyls and hydrogen atoms of imines results in a robust 2D layered structure.[36-39] Additionally, two peaks at 1515 and 1262 cm^{-1} and at 1500 and 1246 cm^{-1} are attributed to

This journal is © The Royal Society of Chemistry 20xx

Please do not adjust margins

Please do not adjust margins

C=N vibrational modes in Zn- and Cu-TABQ respectively, which unambiguously confirm the successful generation of new MOPs.

The simulated Raman and IR spectra of TABQ (Fig. S4a-b and Table S1†) are dominated by the C=O stretching and ring C=C stretching bands around 1690 and 1650 cm^{-1}, respectively, which exhibit minimal changes upon the complexation of TABQ with Zn ions (Fig. S5† and Tab. S2†). The shift from 1664 to 1580 cm^{-1} observed experimentally in the FTIR spectra of Zn and Cu-TABQ is probably associated with the multilayer structure and the hydrogen bonding in the real system and these two effects are not considered in these calculations on the isolated molecules. In full agreement with the experimental IR and Raman analyses, the signals of TABQ associated to the NH_2 group (around 1560 cm^{-1}) disappear in the complex, changing to a combination of C-C and C=N bands (around 1470 cm^{-1}). Similarly, the six-membered ring deformation band of TABQ, around 1320 cm^{-1}, splits upon the formation of the complex. These bands in the central region become dominant in the complex and change significantly the profiles of both IR and Raman spectra. Therefore, ssNMR analysis together with the remarkable similarity between the predicted and experimental FTIR and Raman spectra of TABQ and Zn-TABQ provide unequivocal evidence of the proposed structures, effectively discarding the formation of C=NH groups.

The chemical states of Zn, Cu, N, and O in Zn-TABQ and Cu-TABQ are identified by X-ray photoelectron spectroscopy (XPS) analysis in Fig. S6-8. In the N1s XPS spectra of Zn- and Cu-TABQ in Fig. S7a† and S8a†, there is an extra peak at 398.0eV, attributed to the quinoid imine (C=N), in comparison to the single peak at 399.6 eV, attributed to benzoidamine (C-N) of pure TABQ (Fig. S9†). [24, 40] The clear signal of carbonyl groups in the O1s XPS spectra (See Fig. S7b and S8b) suggests no involvement in the coordination with Zn^{2+} and Cu^{2+}. Fig. S7c and S8c exhibit the typical peaks at 1021 and 1044 eV of Zn^{2+} and 932, 934, 952 and 954 eV of Cu^{2+}.

Elemental analysis (Tab. S3-4) shows that the ratio of Zn^{2+} / Cu^{2+} and N is approximately 1:4 for both Zn-TABQ and Cu-TABQ. This suggests that Zn^{2+} and Cu^{2+} are bonded to TABQ *via* coordination with four N atoms of two TABQ units.

Scanning electron microscopy (SEM) is then used to analyze the MOPs morphology. Fig. 2c-d reveal that the Zn- and Cu-TABQ polymers possess a homogenous 3D network structure when compared to the pristine TABQ (Fig. S10†).

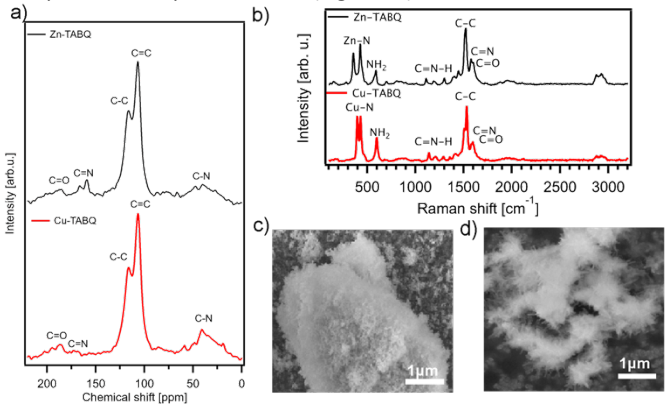

Fig. 2. a) ^{13}C DP-MAS solid-state NMR and b) Raman spectrum of Zn-TABQ (black curve) and Cu-TABQ (red curve). c-d) SEM images of c) Zn-TABQ, and d) Cu-TABQ.

The electronic structure of the bulk Zn-TABQ complex is then investigated by density functional theory (DFT) calculations. The computed projected density of state (PDOS) of Zn-TABQ (Fig. S11†) shows, on the one hand, a significant overlap between N-2p, O-2p and C-2p orbitals as a consequence of the high electron delocalization along the molecular framework. On the other hand, the large overlap between the 2p orbitals of the N atoms and the 3d orbitals of the Zn atoms indicates the strong interaction associated with the formation of Zn-N bonds in the complex. Furthermore, the differential charge density analysis of Zn-TABQ (Fig. S12†), computed as $\Delta\rho$ = ρ[Zn-TABQ] – (ρ[TABQ] + ρ[Zn], reveals that the electron density redistribution upon complex formation primarily occurs in the bonding region between the nitrogen and zinc atoms. This accumulation of charge supports the square planar coordination of the Zn^{2+}. Finally, the electronic band structure of Zn-TABQ along with the high symmetry points of the first Brillouin zone (Fig. S13†) reveals several bands crossing the Fermi level (Γ-C, Γ-V_2), which indicates the metallic character of Zn-TABQ.

The crystalline structure of Zn- and Cu-TABQ is analyzed by powder X-ray diffraction (PXRD) (Fig. 3, S14-16 and Tab. S5-6). The crystalline structure of Zn-TABQ is simulated based on the work of Wang *et al*.[24] but substituting Ni^{2+} for Zn^{2+} ions, and then refined the structure by Rietveld method. The refined unit cell is a monoclinic crystal system with space group C 2/m and the following unit cell parameters a = 11.945 Å, b = 7.641 Å, c = 3.844 Å, α = γ = 90.00°, β = 93.24°. The obtained results are portrayed in Fig. 3a-c, whereas the detailed crystallographic data are displayed in Table S5-6†. The diffraction peaks at 13.75°, 14.84°, 23.16°, 23.26°, 25.23°, 26.66°, 28.33°, are assigned to the (110), (200), (001), (020), (310), (111) and (201) planes, respectively. The experimental PXRD pattern of Zn-TABQ (Fig. 3a, black spectrum) is in good agreement with the calculated pattern, indicating a good crystallinity. It also differs significantly from the one of pure TABQ (Fig. S14†).

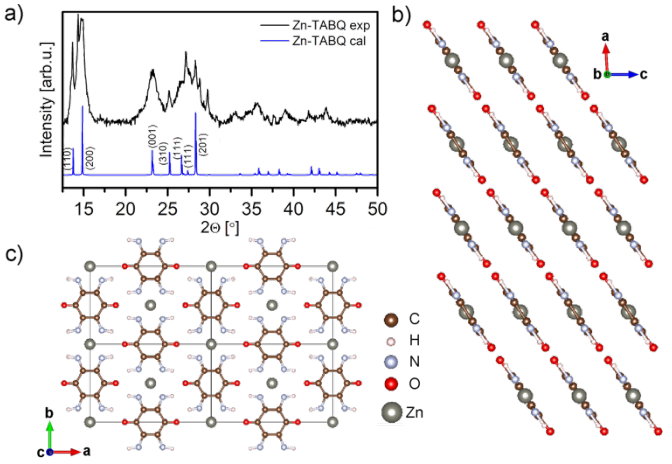

Fig. 3. a) PXRD spectra of Zn-TABQ (black-experimental and blue simulated), b) layered and (c) planar monoclinic packing of Zn-TABQ.

The *d*-spacings calculated from Bragg law correspond to 3.1 Å (001 plane – interlayer 2D plane spacing), and the distance between the Zn^{2+} ions of the neighboring MOP layers is 3.8 Å (201 plane) (Fig 3b). The remaining planes are related to the rigid H-bonded structure[23] and the π-π stacking between aromatic planes of Zn-TABQ.[41] On the other hand, the experimental crystalline structure of Cu-TABQ is similar to the one of Zn-TABQ (Fig. S16) with broad signals at *ca*. 23° and 27°, corresponding to (001) and (201) planes, respectively, meaning that the 1D chains of Cu-TABQ are oriented along the X cell axis plane (201). The main difference lies in the lack of signals related to the (110) and (200) planes (Fig. S16), which clearly indicate a less organized structure compared to Zn-TABQ.

Please do not adjust margins

Please do not adjust margins

The enhanced thermal stability of Zn- and Cu-TABQ is assessed by thermogravimetric analysis (TGA) analysis (Fig. S17†) showing values T_{d10} (thermal decomposition of 10% weight) of approximately 341 and 316 ºC, respectively. The porosity of Zn- and Cu-TABQ is evaluated by recording N_2 adsorption-desorption isotherms at 77 K (Fig. S18-19† and Table S7†) in their completely activated state, *i.e.,* after treating the samples under vacuum (<1 torr pressure) and heating at 100°C for 12 h. The different parameters calculated from Brunauer-Emmett-Teller (BET) can be seen in Table S7†. Interestingly, although the surface area (Fig. S18†) of Cu-TABQ (172 m^2/g) is higher than the one of Zn-TABQ (92 m^2/g), the pore size distribution (Fig. S19†) shows the dominance of micropores for Cu-TABQ (average pore size 3.72 nm) and meso and macropores for Zn-TABQ (average pore size 28.95 nm). The smaller pore size distribution obtained for Cu-TABQ is in full agreement with PXRD analysis, which showed that Cu-TABQ possesses a less ordered structure than Zn-TABQ as well as with FTIR analysis where a weaker NH---O=C H-bonding in Cu-TABQ was observed (Fig. S3†). This can be partially attributed to varying coordination tendencies of Zn^{2+} *vs* Cu^{2+} ions. These findings envisage a higher electrochemical performance for Zn-TABQ MOP.

Electrochemical analysis

Three-electrode system

Prior to the electrochemical characterization of TABQ-based MOPs we assess and compare the solubility of TABQ monomer and Zn-TABQ in the selected ionic liquid, EMIMCl/PC. It is accurate to state that the TABQ monomer, characterized by high symmetry and low dipole moments, exhibits limited solubility in a 1M aqueous $ZnSO_4$ electrolyte.[22] However, in 1M EMIMCl/PC electrolyte, TABQ demonstrates significantly higher solubility, which is quantified to 66 mmol/L, in contrast to its solubility of 1.7 mmol/L in 1M $ZnSO_4$, as determined through UV-vis characterization (Fig. S20†). Then, electrodes utilizing TABQ and Zn-TABQ materials are fabricated and are subsequently immersed in the aforementioned IL for few hours. As can be clearly observed in Fig. S21†, TABQ electrode dissolves and stains the separator, making electrochemical testing impossible compared to Zn-TABQ material which is remarkably insoluble.

The electrochemical performance of Zn and Cu-TABQ samples is first assessed in a three-electrode system using Zn or Cu-TABQ deposited on glassy carbon as working electrode, graphite as counter electrode, Hg/Hg_2Cl_2 as reference electrode and 1 M EMIMCl/PC as electrolyte. Fig. S22a-b shows the CV curves of Zn and Cu-TABQ electrodes, where Zn-TABQ shows nearly rectangular CVs with small redox peaks and Cu-TABQ electrodes show a distinct pair of peaks at 0.7/1.2 V, which is originated from the Cu^{2+}/Cu^{+} couple. At the same scan rate, the specific capacitances of Zn and Cu-TABQ are correlated with the scanning areas of the CV curves. It can be easily observed that the area of Zn-TABQ is greater than that of Cu-TABQ, indicating the former with higher specific capacitance. In particular, the highest specific capacitance for Zn-TABQ amounts to 330 F/g at 2 mV/s of scan rate and to 260 F/g for Cu-TABQ at the same scan rate.

Symmetric cells

The electrochemical performance of Zn- and Cu-TABQ is then evaluated in a symmetric cell using 1 M EMIMCl/PC ionic liquid solution as the electrolyte (Fig. S23-24†). Testing electrode materials in symmetric cells, where both the cathode and anode consist of the same material, offers several key advantages. For instance, by eliminating external factors from different materials, it enables a direct assessment of the material's inherent properties. Symmetric cells facilitate the identification of the dominant charge storage mechanism within the material, whether it relies on electric double-layer capacitance (EDLC), pseudocapacitance, or a combination of both. Furthermore, they provide a clear means to assess the material's rate capability, long-term stability and cyclability. Fig. S23a-b shows the representative cyclic voltammetry (CV) curves of Zn- and Cu-TABQ in the range of 0-2 V with scan rates from 2 to 20 mV/s. Large and nearly rectangular CVs with small redox peaks are observed for Zn- and Cu-TABQ MOPs due to the pseudocapacitive contribution of the carbonyl groups of TABQ. The galvanostatic charge/discharge (GCD) curves of both MOPs (Fig. S23c-d) show a distorted triangular shape, typical of pseudocapacitors. The specific capacitances of both MOPs are calculated from GCD curves at different current densities (see eq. 3). The maximum specific capacitances obtained are 298 and 138 F/g at 0.1 A/g current density for Zn- and Cu-TABQ, respectively.

The electrochemical impedance spectroscopy (EIS) data is analysed using Nyquist plots (see Fig. S23e and S24†). As depicted in Fig. S25e† a semicircle is observed within the high-frequency region representing the foremost supercapacitor's resistive nature, which consists of an electrode/electrolyte/current collector. The nearly vertical line at the low-frequency region reflects an excellent capacitive behavior of both electrodes. The experimental results are well fitted with the two indicated circuits (Fig. S24†). The fitting parameters are reported in Tab. S8†. The magnitude of the R_{ct} for both MOPs is as low as ~100 Ω and the ionic conductivity amounts to ~0.10 S/m. The low charge-transfer resistance indicates that both MOP samples possess a good rate capability.

Finally, to investigate the electrochemical stability of the two MOPs in a symmetric cell, GCD cycling is performed at a current density of 1 A/g (Fig. S23f†). After 5000 cycles, the capacitance decay is below 10% for Zn-TABQ and 20% for Cu-TABQ, respectively, indicating that both MOPs have excellent cycle robustness.

Comparison between Zn and Cu-TABQ electrodes

By and large, the electrochemical performance of Zn-TABQ exceeds the one of Cu-TABQ in both, three-electrode system and symmetric cells. Both MOPs have in common the same core, TABQ, which has the capacity to store charges through its redox-active carbonyl groups. The main difference lies in the central metal ion, Zn^{2+} or Cu^{2+}. Although both metal ions can interact with the electrolyte ions through a capacitive mechanism, we anticipate that Zn^{2+} will remain redox inactive, while Cu^{2+} will exhibit redox activity within the applied potential window.[42] While it is possible that the redox activity of Cu^{2+} might enhance the capacitive contribution of Cu-TABQ MOP, it is essential to take other factors into account as well. The electrochemical performance of an electrode material is influenced by various physical properties, including: surface area, porosity, electronic conductivity, ionic conductivity, ion accessibility, crystal structure, redox active sites and chemical stability.[43, 44] Cu-TABQ MOP exhibits both increased redox activity (Cu^{2+} and TABQ) and a larger surface area (172 m^2/g) in comparison to Zn-TABQ (TABQ and 92 m^2/g, respectively). Nonetheless, the crucial factor appears to be the higher porosity of Zn-TABQ (dominance of meso and macropores, average pore size 28.95 nm), which enhances accessibility to the redox-active carbonyl groups of TABQ and subsequently boosts the electrode performance. In the Cu-TABQ system (dominance of micropores, average pore size 3.72 nm), the poor porosity restricts ionic diffusion and storage, leading to inadequate mass transfer times, especially at high current densities. Furthermore, the exceptional crystallinity of Zn-TABQ contributed to its notable ionic conductivity, which amounts to 0.12 S/m. This value is approximately 40% higher than the ionic conductivity of the Cu-TABQ electrode (0.08 S/m) (Tab. S8†). The additional

 This journal is © The Royal Society of Chemistry 20xx

Please do not adjust margins

Please do not adjust margins

oxidation/reduction of the Cu^{2+} ion in Cu-TABQ can also result in changes in the coordination number or metal ion geometry, leading to a worse chemical stability. Therefore, the lack of redox activity of Zn^{2+} endows Zn-TABQ MOP with higher chemical stability, which is also reflected in the superior long-term cyclability of Zn-TABQ electrodes (Fig. S23f†).

Al-batteries

To further investigate the electrochemical performance of the MOPs electrodes for practical applications as cathode materials in aqueous RABs, a single electrode with a mass loading of ~1 mg/cm² is assembled in a Swagelok-type cell with an Al anode by using $AlCl_3$–EMIMCl IL as electrolyte. Fig. 4a-b and S27 display the CV and GCD curves of Zn- and Cu-TABQ, between 0 and 2.1 V and at scan rates from 1 to 20 mV/s or current densities from 0.1 to 1 A/g, respectively. Analogously to the symmetric two-electrode configuration, the GCD curves show a distorted triangular shape without a clear voltage plateau. As illustrated in Fig. 4a, CV profile of Zn-TABQ exhibits slight variations between Al battery cells (electrolyte $AlCl_3$-EMIMCl) and symmetric cells (electrolyte EMIMCl/PC). Different electrolytes have distinct properties, such as ionic conductivity, ion mobility, and redox potential, which can impact the electrochemical behavior of the electrode material. These variations in electrolyte properties can lead to changes in the shape, position, and intensity of the peaks in the CV profile, making it an essential factor to consider when studying the electrochemical performance of materials. Fig. 4a displays three prominent reduction peaks, and less distinct oxidation peaks. Although the absence of clear oxidation peaks may be attributed to irreversible reduction processes, similar behavior has been observed for other systems where the kinetics of electron transfer during the reduction process are significantly faster than during the oxidation process. As a result, the reduction peak may be more pronounced and easier to detect. To ascertain the reversibility of the redox processes in the TABQ-based MOPs, we conducted five consecutive CV curves for Zn-TABQ using a scan rate of 50 mV/s. The remarkable similarity among the five CV curves attests to the complete reversibility of the redox processes in the Zn-TABQ electrodes.While the CV profiles of Zn-TABQ show three redox peaks above 0.9V , attributed to the redox active carbonyl and imine groups and to the Al-based compounds insertion, the CV profile of Cu-TABQ (Fig. S25†) shows two additional redox peaks in the voltage region of 0-0.8V, which can be attributed to the redox chemistry of Cu^{2+} ions (*i.e.,* $Cu^{2+}\leftrightarrow Cu^{+}$ and $Cu^{+}\leftrightarrow Cu$).

To shed light on the nature of the charge storage mechanism of both MOPs, the kinetics of the electrochemical processes occurring at both electrode materials is determined by exploiting the procedure proposed by Wu *et al*., (see Fig. S27†).[45] The relation of the peak current (I) and scan rate (v) from CV complies with the equation:

$$i = av^b \quad \text{(eq. 1)}$$

The average values of b for Zn- and Cu-TABQ are 0.55 and 0.60, respectively. A predominantly diffusion-controlled contribution in the charge storage mechanism of both MOPs is obtained, as well as a partial capacitive contribution (i.e., from the central metal ion), which is higher in the case of Cu-TABQ as expected from its smaller pore size distribution. To further analyze the capacitive contribution and the diffusion-controlled contribution at a specific scan rate, the equation (1) can be divided into two parts:

$$i = k_1v + k_2v^{1/2} \quad \text{(eq. 2)}$$

where k_1v and $k_2v^{1/2}$ represent the capacitive and diffusion limited effects, respectively. The capacitive and diffusion-controlled capacity values at different rates are calculated and shown in Fig. S28 and Fig. S31 for Zn and Cu-TABQ, respectively. As shown in Fig. S28 and S29 the diffusion contribution to the charge storage mechanism for the Cu-TABQ is the highest (80.07%) at the highest scan rate (20 mV/s). The capacitive contribution gradually increases with the scan rate for both Zn and Cu-TABQ. This result confirms the hybrid nature of Zn and Cu-TABQ, with the coexistence of an electrical double layer (EDL) and battery-type mechanism due to the pseudocapacitive nature provided by the carbonyl groups.

Subsequently, the capacity of Zn and Cu-TABQ MOPs is calculated from the GCD analysis between the adopted potential window, showing that the Zn-TABQ (Fig. 4c) cathode displays a significantly high discharge capacity of 198 mAh/g compared to 57 mAh/g of Cu-TABQ (Fig. S30) at the current density of 0.05 A/g and 0.1 A/g respectively. Besides, Zn-TABQ displays an outstanding maximum energy density of 247 Wh/kg which is superior to Cu-TABQ (63 Wh/kg) and to all the previously reported common cathode materials in Al-batteries (Tab. S9†).

The higher performance of Zn-TABQ indicates a more efficient utilization of the carbonyl active sites than in Cu-TABQ, which is in full agreement with the symmetric cell analysis and is mainly attributed to the larger pore size distribution of Zn-TABQ. Besides, the obtained capacity of Zn-TABQ is very close to the theoretical value (see in Supporting Information the calculation). A good rate capability is achieved for both MOPs where capacity values of 154, 111.8, 97.5, 92.1, mAh/g for Zn-TABQ and 55.6, 48.8, 35, 27.6, mAh/g for Cu-TABQ are obtained at a current density of 0.1, 0.2, 0.5, 1 A/g, respectively. The long-term charge and discharge tests (Fig. 4d and S22d) provide evidence for the high cyclability of Zn- and Cu-TABQ cathodes at a high current density of 1 A/g, which can retain a 92.2% and 84.1%, respectively, of the initial capacity value after >5000 cycles.

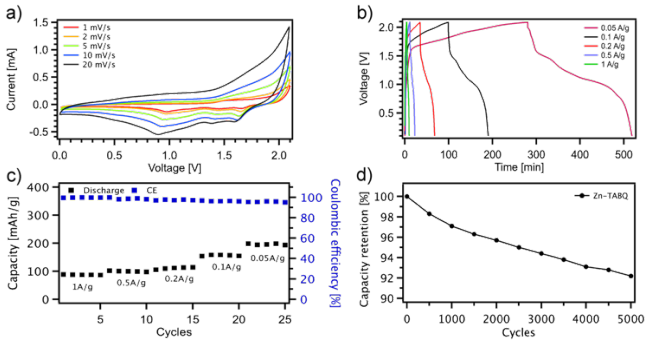

Fig. 4. Electrochemical characterization of Zn-TABQ in Al-battery configuration. a) CV curves at different scan rated, b) GCD curves at different current densities, c) specific capacity as a function of the current densities, d) cycling stability.

Charge storage mechanism in Al-batteries

To elucidate the charge storage mechanism of Zn-TABQ-based electrodes in RABs (Fig. 5a), ex situ FT-IR, XPS and Raman spectroscopy are performed in pristine (1.31V for Zn-TABQ and 1.28V for Cu-TABQ), charged (2.0 V) and discharged (0.1 V) states (Fig. 5 and S33-38). The storage mechanism of cationic aluminium complexes, specifically $[AlCl_x]^{(3-x)}$ where x is 1 or 2, as proposed by RABs, differs from that of traditional $AlCl_4^-$ or Al^{3+}species. The specific composition of aluminum complex ion $[AlCl_x]^{(3-x)}$ is influenced by factors such as the nature of the electrolyte, the structure of the cathode materials, the occurrence of a redox reaction, and the charge carried by the particular group.[46] The ionic liquid electrolyte -

Please do not adjust margins

Please do not adjust margins

ethyl-3-methylimidazolium aluminum chloride ($AlCl_3$[EMIm]Cl) is typically governed by the chemical equilibria[13, 47, 48]:

$$\boldsymbol{AlCl_3 + [EMImCl] \rightarrow AlCl_2^+ + 2AlCl_4^- + EMIm^+} \quad (1)$$

$$\boldsymbol{AlCl_3 + AlCl_4^- \rightarrow Al_2Cl_7^-} \quad (2)$$

The cathode materials will interact with the positively charged species ($AlCl_2^+$ and $EMIm^+$) during the discharging process, and with the negatively charged species ($Al_2Cl_7^-$ and $AlCl_4^-$) during the charging process.

The FT-IR spectrum of discharged Zn-TABQ (Fig. 5a, blue spectrum) reveals the disappearance of the C=O stretching vibration at 1580 cm^{-1}, together with the appearance of a C-O stretching vibration at 1236 cm^{-1} and the O-Al stretching vibration at 1032 cm^{-1}.[29] During the discharging process, carbonyl groups accept electrons and are reduced to $C\text{-}O^-$ anions, which subsequently coordinate with the available cations in the media to compensate the negative charge.[49, 50] The reduction process also converts the conjugated quinone ring (pristine and charged states) to a π-conjugated benzene ring (discharged state). Quinone structure exhibits symmetric double bonds in the six-membered carbon ring, which results in a larger dipole moment change of the anti-symmetric stretching vibration and therefore a stronger IR absorption is observed at 1647 cm^{-1} (C=C). The FT-IR spectrum of Zn-TABQ in the charged state (Fig. 5b red spectrum) resembles the one of the pristine electrode, confirming the reversible nature of the redox carbonyl groups and the transition between conjugated structures.

To determine the species involved in the electrochemical reactions, high-resolution O1s, Al2p, Zn2p, and N1s XPS analyses are then performed. In full agreement with ex situ FTIR, in the high-resolution O1s spectra (Fig. 5c), the peak intensities of C=O at 531.86 eV and C-O at 533.0 eV change cyclically during the electrochemical reactions, which further confirms the redox-active nature of the carbonyl groups. In the N1s spectra (Fig. S31†), when Zn-TABQ electrode is discharged to 0 V, the peak of quinoid imine (C=N) at 398.0 eV is diminished and simultaneously a new peak at 401.9 eV appears, corresponding to the $EMIm^+$ ammonium salt. Both the conjugated benzoid carbonyls and imines are reversibly oxidized in the following charging process, as shown in the O1s and N1s XPS spectra in Fig. 5 and Fig. S31, respectively. The high-resolution Al2p spectra (Fig. 5) reveal the peak at 75.0 eV, which exhibits a higher intensity in the discharged state, but it is also present in the charged state. To shed light on the aluminum complex ions present, the ratio between Cl and Al is calculated from the survey spectra (Fig. S32†). While the charged cathode exhibits a Cl/Al ratio of 3.5, indicating that the major Al-species coordinating to Zn-TABQ is $Al_2Cl_7^-$, the Cl/Al ratio in the discharged state amounts to 2, indicating that $AlCl_2^+$ is the dominant Al-species. To confirm the solely presence of $Al_2Cl_7^-$ as negatively charged Al-species, ex situ Raman analysis is performed on the Al anode (Fig. 5c). As can be seen in Fig. 5c, while multiple signals of $EMIm^+$ can be observed in the charged state, the discharged state spectrum is dominated by the signal of $Al_2Cl_7^-$ at 310 cm^{-1},[47] and not $AlCl_4^-$, confirming that the overall reaction of the electrolyte as:

$$\boldsymbol{AlCl_3 + [EMImCl] \rightarrow AlCl_2^+ + Al_2Cl_7^- + EMIm^+} \quad (3)$$

Ex situ Raman spectroscopy (Fig. S33†) is also performed on the cathode to confirm the chemical stability of Zn-TABQ upon the charging and discharging process. Importantly, the high-resolution Zn2p spectra (Fig. S34†) and the Raman spectra (Fig. S35†) confirm that Zn^{2+} is not involved in the redox processes, as no valence changes are observed in the operating potential window ($Zn^{2+} \leftrightarrow Zn$, $E^0 = -0.7618V$).

The redox centers in the discharge/charge process of Zn-TABQ are further confirmed by DFT calculations in Fig. 5d and Fig. S35. Upon the addition of two electrons to a Zn-TABQ unit, the theoretical calculations indicate that most of the electron density accumulates on the molecular framework, especially on the atoms of the carbonyl group and on the nitrogen atoms as depicted in Fig. S35a† and 5d. A similar trend is also observed when two additional electrons are added (Fig. S35b† and 5d), being the most significant change that the extra electron density accumulates appreciably on the carbon aromatic atoms. Overall, we have demonstrated that the benzoid carbonyls are the redox centers and responsible for the uptake of $AlCl^{2+}$ and $EMIM^+$ during the discharging process. Conversely, during the charging process, the Zn-TABQ cathode interacts with the negatively charged $\boldsymbol{Al_2Cl_7^-}$. A summary of the charge storage mechanism can be seen in Figure S36, specifically, the interactions of the different electrolyte ions with the Al anode and the Zn-TABQ cathode during the charging/discharging processes.

This journal is © The Royal Society of Chemistry 20xx

Please do not adjust margins

Please do not adjust margins

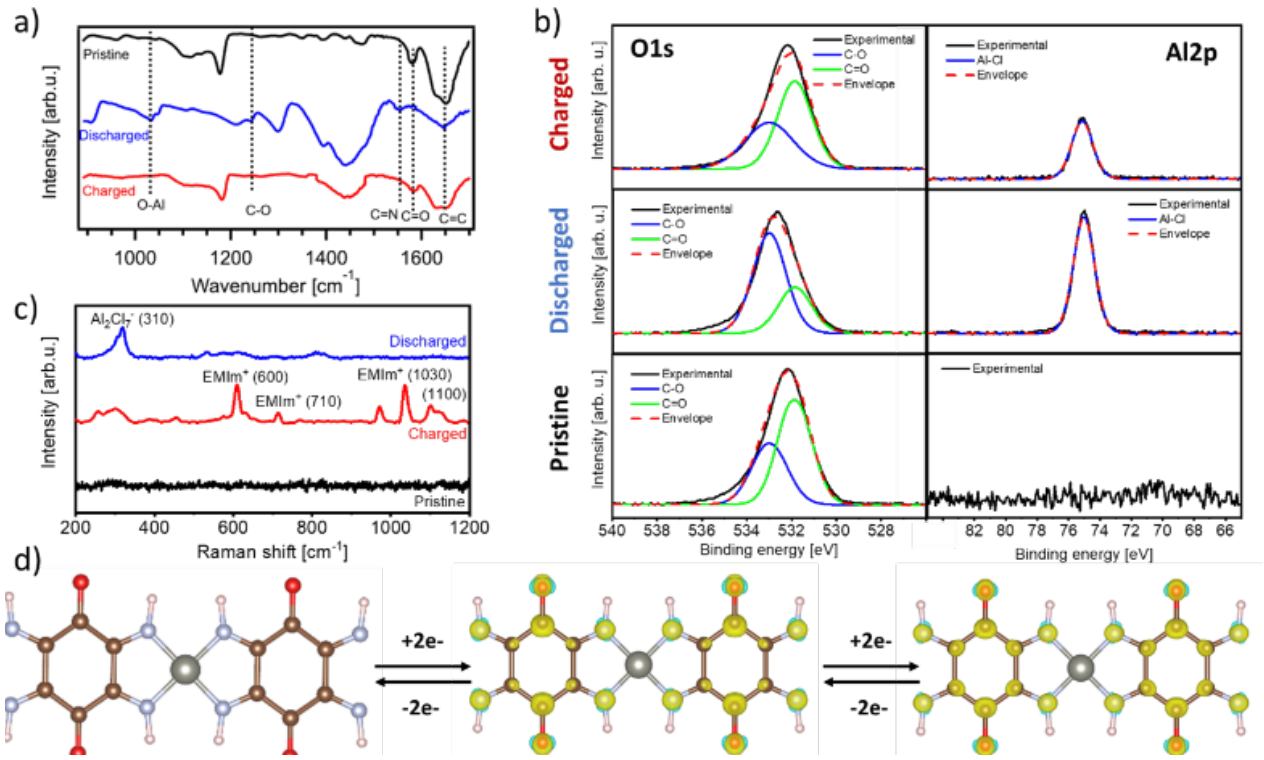

Fig. 5. Ex situ measurements for pristine, discharged and charged form of Zn-TABQ a) FT-IR b) XPS (O1s and Al2p), c) Raman spectroscopy, d) DFT calculations. Pristine and successive charge density changes after the addition of two electron and four electrons to a Zn-TABQ unit. The yellow regions present an increase of the charge density and the cyan color represent zones with a reduction of the charge density. The isosurface value is set to 0.004 *e* bohr^{-3}.

Conclusions

In summary, we have synthesized two novel MOPs, *i.e.*, Zn- and Cu-TABQ, via the coordination between benzoid imines of TABQ and Zn^{2+} or Cu^{2+} metal ions, respectively. The polymer chains of Zn-TABQ and Cu-TABQ are linked by hydrogen bonds between the oxygen atoms of benzoid carbonyls and hydrogen atoms of imines to form a robust 2D layered structure. The MOP Zn-TABQ, whose pore size distribution is dominated by meso and macropores, possess a higher ionic conductivity, and a redox-inactive metal ion, exhibited a better electrochemical performance than Cu-TABQ, whose pore size distribution is dominated by micropores, and the redox activity of its metal ion resulted in a lower chemical stability. Specifically, Zn-TABQ displayed a high capacitance (298 F/g) and long cycling stability (capacitance retention of 90% respectively, after >5000 cycles) in a symmetric system, as well as a high capacity, equal to 198 mAh/g at 0.05 A/g and extraordinary cycling stability at 1 A/g with 92 % retention, after 5000 cycles in aqueous RABs. Moreover, Zn-TABQ possesses an outstanding energy density of 247 Wh/kg, the highest value reported for cathode materials in Al-batteries. Finally, we demonstrated *via* ex situ analysis and DFT calculations that conjugated carbonyl groups act as the redox-active centers for the coordination with $AlCl_2^+$ and $EMIM^+$ electrolyte ions. All in all, the coordination chemistry approach for rational design of novel and versatile redox-active MOPs is demonstrated being a powerful strategy to boost the electrochemical performance of Al-batteries and beyond.

Experimental section

Synthesis of Zn-TABQ and Cu-TABQ

The TABQ monomer was synthesized by following a previously reported methodology.[22] Briefly, 297 mg (0.1 mmol) of zinc nitrate hexahydrate or 241 mg copper (II) nitrate trihydrate and 2 ml of concentrated aqueous ammonia (~14 M) were added to 30 ml of dimethyl sulfoxide with 168 mg (0.1 mmol) of TABQ under vigorous stirring. The reaction was kept under stirring for 3 hours under ambient conditions at room temperature. The solid was soaked in deionized water (200 ml) and thoroughly washed with deionized water and acetone for several times and then dried at 80 °C in an oven for 12 h. Yield: 219 mg (94%) for Zn-TABQ and 207 mg (90%) for Cu-TABQ.

Material Characterization:

^{13}C NMR spectra of TABQ, Zn-TABQ and Cu-TABQ were carried out on a Bruker Avance III HD NMR spectrometer. The Powder X-ray diffraction (PXRD) patterns were recorded on X-ray diffractometer Bruker ASX D8 Advanced with Cu Kα line focused radiation (λ = 1.5405 Å). Surface areas and porosity were measured by nitrogen adsorption and desorption at 77 K using a Micromeritics ASAP 2050 and the samples were degassed at 100 °C for 12 h under vacuum before analysis. Fourier infrared spectrometer FT-IR-4700 JASCO with ATR Diamond attachment was used to characterize the infrared spectrum with the mid-IR range 400–3500 cm^{-1}. The thermogravimetric analysis (TGA) of all samples were evaluated with a Mettler Toledo TGA/SDTA851e system over the temperature range from 25 to 1000 °C under N_2 atmosphere at a heating rate of 5 °C min^{-1}. Scanning electron microscopy (SEM) micrographs were recorded on an FEI Quanta 250 FEG Scanning Electron Microscope operating at an accelerating voltage of 5 keV incident beam energy.

Please do not adjust margins

Please do not adjust margins

X-ray photoelectron spectroscopy (XPS) was performed using a Thermo Scientific KAlpha X-ray photoelectron spectrometer with a monochromatized Al Kα anode as X-ray source (1486 eV). The composition analysis was performed using Vario EL III Elementary Analyser. Raman spectra measurements collected using a Raman spectrometer were recorded by a Renishaw microscope with a 100× objective. The crystallographic features as an atomic arrangement and structure parameters were generated and visualized by VESTA software.[51] The lattice parameters of the crystal structure were determined from Rietveld refinement to the experimental XRD data by use Material Analysis Using Diffraction (MAUD) software.[52]

Computational methods

Geometrical optimization of isolated structures of TABQ and its Zn-TABQ complex were performed using density functional theory (DFT) at the M062X/6-311++G** level, followed by analysis of their vibrational frequencies to characterize the structures obtained as energy minima. These computations were performed using Gaussian16.[53] The description for the vibrational modes and its assignment to the theoretical IR and Raman spectra was performed by visual inspection of the atomic displacements for each vibrational mode in combination with the results from the VEDA program, which generates an optimized set of internal coordinates based on the molecular structure and provides a potential energy distribution for the quantitative analysis of vibrational spectra.[54] DFT calculations on periodic models of TABQ and Zn-TABQ were performed using the Vienna Ab initio Simulation Package (VASP).[55, 56] The PBE exchange−correlation functional was employed with the projected augmented wave (PAW) method to describe the core electrons and plane waves with a kinetic cutoff of 520 eV to describe valence electrons. The experimental 1 x 1 x 1 bulk cell was used for the calculation of electronic properties along with a Γ-centered 5 × 8 × 15 Monkhorst–Pack *k*-point mesh. The VASPKIT code was used for post-processing these calculations.[57]

Electrochemical measurements:

The electrochemical performance of the Zn-TABQ and Cu-TABQ electrodes including cyclic voltammetry (CV), galvanostatic charge/discharge (GCD) profiles and electrochemical impedance spectroscopy (EIS) were evaluated in CR2032 type coin cells and SWE Swagelok at room temperature.

Electrodes preparation and electrochemical measurements

Electrochemical measurements: CVs and GCD curves were recorded using EC-LAB VMP3 (BioLogic Science Instrument).

Fabrication of working electrodes: The working electrodes were prepared by mixing of Zn-TABQ or Cu-TABQ (80% wt, 16 mg), carbon black (10% wt, 2 mg) and PTFE (10% wt, 2 mg) in agate mortar with several drops of NMP to obtain a homogenous paste. The paste was then coated into a carbon paper electrode with diameter of 1.6 cm and further dried under vacuum at 80° C. The mass loading of the Zn-TABQ or Cu-TABQ was ~1 mg/cm^2 in each electrode.

Fabrication of symmetrical two-electrode configuration: Two electrodes were assembled in CR2032 stainless steel coin-type cells with a porous cellulose membrane as separator and 1M 1-Ethyl-3-methylimidazolium chloride in propylene carbonate as electrolyte.

Electrochemical characterization of the symmetric cell: CV was performed in the voltage range from 0 to 2.1 V using scan rates ranging from 1 to 20 mV/s. GCD was performed in the same voltage window using current densities varying from 0.05 to 1 A/g. Cyclability tests were performed through GCD measurements at 1 A/g scan rate for 5000 cycles in the same potential window.

Fabrication of Al-batteries: The working electrodes were prepared according to the following procedures. Zn-TABQ or Cu-TABQ (60 wt%, 24 mg) were mixed with carbon black (30 wt%, 12 mg) and PTFE (10 wt%, 4 mg) in agate mortar with several drops of NMP to obtain a homogenous paste. The resultant slurry was then coated into a carbon fibre electrode with diameter of 0.8 cm and further dried under vacuum at 80° C. The mass loading of the Zn-TABQ or Cu-TABQ was ~1 mg/cm^2 in each electrode.

Electrochemical characterization of Al-batteries: Two-electrode Swagelok cells with tungsten rod were assembled in glove box to evaluate the electrochemical performance of Al-batteries. A circular cathode electrode was stacked with a glass fiber separator (Merck) and Al foil anode, and then wetted by $AlCl_3$/[EMIM]Cl ~1.3 as electrolyte. A steel spacer and spring were added afterword and sealed well for electrochemical measurement.

Electrochemical calculations

Calculation of the specific capacitances: The specific capacitance was calculated using GCD with following equation:

$$C_s = \frac{2 \cdot I \cdot \Delta t}{\Delta V \cdot m} \quad \text{(eq. 3)}$$

Where, I (A) is the response current, Δt (s) is the discharge time, ΔV (V) is the voltage window and m (g) is the mass of Zn-TABQ or Cu-TABQ in a single electrode.

Calculation of the specific capacities: The specific capacity was calculated using GCD with following equation:

$$C = \frac{I \cdot \Delta t}{3.6 \cdot m} \quad \text{(eq. 4)}$$

Where, I (A) is the applied current, Δt (s) is the discharge time, and m (g) is the mass of Zn-TABQ or Cu-TABQ in a single electrode (cathode).

Power and energy density calculations

The energy density of the device was obtained from the formula:

$$E = \frac{1}{2} \cdot C \cdot \frac{(\Delta V)^2}{3.6} \quad \text{(eq. 5)}$$

The power density of the device was calculated from the formula

$$P = \frac{E}{\Delta t} \cdot 3600 \quad \text{(eq. 6)}$$

Where, *E* is specific energy (Wh kg^{-1}), C is the specific capacitance (F/g), ΔV is the potential window (V), *P* is power density (W kg^{-1}) and Δt is the discharge time (s)

Calculation of ionic conductivity (σ)

$$\sigma = \frac{l}{R_i \cdot A} \quad \text{(eq. 7)}$$

Being l the film thickness (100 µm), A the film area (1.27 cm^2) and Ri is the ionic resistance.

Calculation of the theoretical capacity

Theoretical capacity of the Zn-TABQ was calculated by the Faraday's law:

$$C_0 = nF/M_0 \quad \text{(eq. 8)}$$

Where *n* is the number of electrons transferred (here 4), F is Faraday's constant (96485 C/mol) and M_0 is the relative molecular weight of a Zn-TABQ unit (393.38 g/mol).Therefore, C_0= 4 x 96485 / (3.6 x 393.38)= 272.5 mAh/g

Author Contributions

‡ These authors contributed equally.

Conflicts of interest

The authors declare no competing financial interest.

Acknowledgements

This work was supported by the National Science Centre (grant no. 2020/36/C/ST5/00247; UMO-2020/39/D/ST4/01182). We also acknowledge support from the Interdisciplinary Thematic Institute SysChem via the IdEx Unistra (ANR-10-IDEX-0002) within the program Investissement d'Avenir program, the Foundation Jean-Marie Lehn and the Institut Universitaire de France (IUF).

 This journal is © The Royal Society of Chemistry 20xx

Please do not adjust margins

Please do not adjust margins

References

1. A. Ponrouch, J. Bitenc, R. Dominko, N. Lindahl, P. Johansson and M. R. Palacin, *Energy Storage Mater.*, 2019, **20**, 253-262.
2. R. Wang, M. Yao and Z. Niu, *InfoMat*, 2020, **2**, 113-125.
3. H. Wang, X. Wang, M. Li, L. Zheng, D. Guan, X. Huang, J. Xu and J. Yu, *Adv. Mater.*, 2020, **32**, 2002559.
4. A. Halder, M. Ghosh, A. Khayum M, S. Bera, M. Addicoat, H. S. Sasmal, S. Karak, S. Kurungot and R. Banerjee, *J. Am. Chem. Soc.*, 2018, **140**, 10941-10945.
5. *Communication Critical Raw Materials Resilience: Charting a Path towards greater Security and Sustainability, COM(2020)474*.
6. K. L. Ng, B. Amrithraj and G. Azimi, *Joule*, 2022, **6**, 134-170.
7. D. J. Kim, D.-J. Yoo, M. T. Otley, A. Prokofjevs, C. Pezzato, M. Owczarek, S. J. Lee, J. W. Choi and J. F. Stoddart, *Nat. Energy*, 2019, **4**, 51-59.
8. J. Tu, W.-L. Song, H. Lei, Z. Yu, L.-L. Chen, M. Wang and S. Jiao, *Chem. Rev.*, 2021, **121**, 4903-4961.
9. J. Bitenc, N. Lindahl, A. Vizintin, M. E. Abdelhamid, R. Dominko and P. Johansson, *Energy Storage Mater.*, 2020, **24**, 379-383.
10. M.-C. Lin, M. Gong, B. Lu, Y. Wu, D.-Y. Wang, M. Guan, M. Angell, C. Chen, J. Yang, B.-J. Hwang and H. Dai, *Nature*, 2015, **520**, 324-328.
11. F. Wu, H. Yang, Y. Bai and C. Wu, *Adv. Mater.*, 2019, **31**, 1806510.
12. Y. Lu and J. Chen, *Nat. Rev. Chem.*, 2020, **4**, 127-142.
13. F. Guo, Z. Huang, M. Wang, W.-L. Song, A. Lv, X. Han, J. Tu and S. Jiao, *Energy Storage Mater.*, 2020, **33**, 250-257.
14. L. Kong, M. Liu, H. Huang, Y. Xu and X.-H. Bu, *Adv. Energy Mater.*, 2022, **12**, 2100172.
15. G. Wang, E. Dmitrieva, B. Kohn, U. Scheler, Y. Liu, V. Tkachova, L. Yang, Y. Fu, J. Ma, P. Zhang, F. Wang, J. Ge and X. Feng, *Angew. Chem., Int. Ed. Engl.*, 2022, **61**, e202116194.
16. L. Zhou, Z. Zhang, L. Cui, F. Xiong, Q. An, Z. Zhou, X.-F. Yu, P. K. Chu and K. Zhang, *Cell Rep. Phys. Sci.*, 2021, **2**, 100354.
17. Y.-T. Kao, S. B. Patil, C.-Y. An, S.-K. Huang, J.-C. Lin, T.-S. Lee, Y.-C. Lee, H.-L. Chou, C.-W. Chen, Y. J. Chang, Y.-H. Lai and D.-Y. Wang, *ACS Appl. Mater. Interfaces*, 2020, **12**, 25853-25860.
18. A. Khayum M, M. Ghosh, V. Vijayakumar, A. Halder, M. Nurhuda, S. Kumar, M. Addicoat, S. Kurungot and R. Banerjee, *Chem. Sci.*, 2019, **10**, 8889-8894.
19. Y. Chen, Q. Zhu, K. Fan, Y. Gu, M. Sun, Z. Li, C. Zhang, Y. Wu, Q. Wang, S. Xu, J. Ma, C. Wang and W. Hu, *Angew. Chem., Int. Ed.* , 2021, **60**, 18769-18776.
20. J. Bitenc, U. Košir, A. Vizintin, N. Lindahl, A. Krajnc, K. Pirnat, I. Jerman and R. Dominko, *Energy Mater. Adv.*, **2021**.
21. J. He, X. Shi, C. Wang, H. Zhang, X. Liu, Z. Yang and X. Lu, *Chem. Commun.*, 2021, **57**, 6931-6934.
22. Z. Lin, H.-Y. Shi, L. Lin, X. Yang, W. Wu and X. Sun, *Nat. Commun.* , 2021, **12**, 4424.
23. Q. Lv, Z. Zhu, S. Zhao, L. Wang, Q. Zhao, F. Li, L. A. Archer and J. Chen, *J. Am. Chem. Soc.*, 2021, **143**, 1941-1947.
24. L. Wang, Y. Ni, X. Hou, L. Chen, F. Li and J. Chen, *Angew. Chem., Int. Ed. Engl.*, 2020, **59**, 22126-22131.
25. K. M. Choi, H. M. Jeong, J. H. Park, Y.-B. Zhang, J. K. Kang and O. M. Yaghi, *ACS Nano*, 2014, **8**, 7451-7457.
26. O. M. Yaghi, *J. Am. Chem. Soc.*, 2016, **138**, 15507-15509.
27. C. Wang, G.-Y. Qiao, J.-S. Qin and J. Yu, *J. Solid State Chem.*, 2020, **287**, 121377.
28. K. Fan, C. Fu, Y. Chen, C. Zhang, G. Zhang, L. Guan, M. Mao, J. Ma, W. Hu and C. Wang, *Adv. Sci.* , 2023, **10**, 2205760.
29. G. Ding, L. Zhu, Q. Han, L. Xie, X. Yang, X. Li, L. Chen, G. Wang, F. Sun and X. Cao, *ACS Appl. Energy Mater.*, 2021, **4**, 8538-8549.
30. J. Geng, Y. Ni, Z. Zhu, Q. Wu, S. Gao, W. Hua, S. Indris, J. Chen and F. Li, *J. Am. Chem. Soc.*, 2023, **145**, 1564-1571.
31. A. R. Lim, *AIP Advances*, 2019, **9**, 105115.
32. R. E. Wasylishen and M. R. Graham, *Can. J. Chem.*, 1976, **54**, 617-623.
33. R. E. Wasylishen and J. S. Cohen, *J. Am. Chem. Soc.*, 1977, **99**, 2480-2482.
34. N. Bloembergen and L. O. Morgan, *J. Chem. Phys.* , 1961, **34**, 842-850.
35. F. Calderazzo, F. Marchetti, G. Pampaloni and V. Passarelli, *J. Chem. Soc., Dalton Trans.*, 1999, 4389-4396.
36. C. Qian, L. Feng, W. L. Teo, J. Liu, W. Zhou, D. Wang and Y. Zhao, *Nat. Rev. Chem.*, 2022, **6**, 881-898.
37. A. Natraj, W. Ji, J. Xin, I. Castano, D. W. Burke, A. M. Evans, M. J. Strauss, M. Ateia, L. S. Hamachi, N. C. Gianneschi, Z. A. Alothman, J. Sun, K. Yusuf and W. R. Dichtel, *J. Am. Chem. Soc.*, 2022, **144**, 19813-19824.
38. H. V. Babu, M. G. M. Bai and M. Rajeswara Rao, *ACS Appl. Mater. Interfaces*, 2019, **11**, 11029-11060.
39. C. R. DeBlase, K. E. Silberstein, T.-T. Truong, H. D. Abruña and W. R. Dichtel, *J. Am. Chem. Soc.*, 2013, **135**, 16821-16824.
40. Y. Chen, M. Tang, Y. Wu, X. Su, X. Li, S. Xu, S. Zhuo, J. Ma, D. Yuan, C. Wang and W. Hu, *Angew. Chem. Int. Ed.*, 2019, **58**, 14731-14739.
41. C. Janiak, *J. Chem. Soc., Dalton Trans.*, 2000, 3885-3896.
42. A. Krężel and W. Maret, *Arch. Biochem. Biophys.*, 2016, **611**, 3-19.
43. Z. Song and H. Zhou, *Energy Environ. Sci.*, 2013, **6**, 2280-2301.
44. Y. Liu, Y. Zhu and Y. Cui, *Nat. Energy*, 2019, **4**, 540-550.
45. X. Wu, J. J. Hong, W. Shin, L. Ma, T. Liu, X. Bi, Y. Yuan, Y. Qi, T. W. Surta, W. Huang, J. Neuefeind, T. Wu, P. A. Greaney, J. Lu and X. Ji, *Nat. Energy*, 2019, **4**, 123-130.
46. Z. Huang, X. Du, M. Ma, S. Wang, Y. Xie, Y. Meng, W. You and L. Xiong, *ChemSusChem*, 2023, **16**, e202202358.
47. X. Wen, Y. Liu, A. Jadhav, J. Zhang, D. Borchardt, J. Shi, B. M. Wong, B. Sanyal, R. J. Messinger and J. Guo, *Chem. Mater.*, 2019, **31**, 7238-7247.
48. C. Ferrara, V. Dall'Asta, V. Berbenni, E. Quartarone and P. Mustarelli, *J. Phys. Chem. C*, 2017, **121**, 26607-26614.
49. E. W. Zhao, T. Liu, E. Jónsson, J. Lee, I. Temprano, R. B. Jethwa, A. Wang, H. Smith, J. Carretero-González, Q. Song and C. P. Grey, *Nature*, 2020, **579**, 224-228.
50. Y. Liang, Y. Jing, S. Gheytani, K.-Y. Lee, P. Liu, A. Facchetti and Y. Yao, *Nat. Mater.* , 2017, **16**, 841-848.
51. K. Momma and F. Izumi, *J. Appl. Cryst.*, 2011, **44**, 1272-1276.
52. S. Matthies, L. Lutteroti and H. R. Wenk, *J. Appl. Cryst.*, 1997, **30**, 31-42.
53. *Gaussian 16, Revision C.01; Frisch, M. J.; Trucks, G. W.; Schlegel, H. B.; Scuseria, G. E.; Robb, M. A.; Cheeseman, J. R.; Scalmani, G.; Barone, V.; Petersson, G. A.; Nakatsuji, H.; Li, X.; Caricato, M.; Marenich, A. V.; Bloino, J.; Janesko, B. G.; Gomperts, R.; Mennucci, B.; Hratchian, H. P.; Ortiz, J. V.;*

Please do not adjust margins

Please do not adjust margins

Izmaylov, A. F.; Sonnenberg, J. L.; Williams-Young, D.; Ding, F.; Lipparini, F.; Egidi, F.; Goings, J.; Peng, B.; Petrone, A.; Henderson, T.; Ranasinghe, D.; Zakrzewski, V. G.; Gao, J.; Rega, N.; Zheng, G.; Liang, W.; Hada, M.; Ehara, M.; Toyota, K.; Fukuda, R.; Hasegawa, J.; Ishida, M.; Nakajima, T.; Honda, Y.; Kitao, O.; Nakai, H.; Vreven, T.; Throssell, K.; Montgomery, J. A., Jr.; Peralta, J. E.; Ogliaro, F.; Bearpark, M. J.; Heyd, J. J.; Brothers, E. N.; Kudin, K. N.; Staroverov, V. N.; Keith, T. A.; Kobayashi, R.; Normand, J.; Raghavachari, K.; Rendell, A. P.; Burant, J. C.; Iyengar, S. S.; Tomasi, J.; Cossi, M.; Millam, J. M.; Klene, M.; Adamo, C.; Cammi, R.; Ochterski, J. W.; Martin, R. L.; Morokuma, K.; Farkas, O.; Foresman, J. B.; Fox, D. J. Gaussian, Inc., Wallingford CT, 2016.

54. M. H. Jamróz, *Spectrochim. Acta Part A: Mol. Biomol. Spectrosc.*, 2013, **114**, 220-230.
55. G. Kresse and J. Furthmüller, *Phys. Rev, B*, 1996, **54**, 11169-11186.
56. G. Kresse and J. Furthmüller, *Comput. Mater. Sci.*, 1996, **6**, 15-50.
57. V. Wang, N. Xu, J.-C. Liu, G. Tang and W.-T. Geng, *Comput. Phys. Commun.*, 2021, **267**, 108033.

This journal is © The Royal Society of Chemistry 20xx

Please do not adjust margins